nature communications

Article

https://doi.org/10.1038/s41467-024-54610-6

High-performance multiphase Sm-Co-B alloys with coercivities up to 6.71 MA·m^{-1}

Received: 26 February 2024

Accepted: 15 November 2024

Published online: 23 November 2024

Check for updates

Shu Wang[1], Ji-Bing Sun[1] ✉, Xiang Chi[2] ✉, Mu-Jing Zhou[1], Hao-Yu Ma[1], Ying Zhang[3] ✉ & Jian Liu[4] ✉

$SmCo_4B$-based alloys with high magnetocrystalline anisotropy are expected to be used as raw materials or constituent phases for new permanent magnets. In this work, we develop $Sm(Co, Fe, Ni)_4B$ alloys with excellent hard magnetic properties by tuning the contents of Fe, Co, and Ni. The addition of Fe enhances the amorphous formation ability of the as-spun ribbons, whereas Ni addition improves the structural stability of the crystalline phases. During annealing, the amorphous phase crystallizes into different Sm-Co-B phases in stages. A high coercivity of 5.68–6.71 MA·m^{-1} is obtained in the annealed $SmCo_{4-x-y}Fe_xNi_yB$ ($x = 1.0–2.0$, $y = 0.8–1.0$) ribbons composed of platelet-shaped and equiaxed grains in comparison with the coercivity of 2.89–5.18 MA·m^{-1} in the $x = 1.0–1.2$ and $y = 0–0.8$ ribbons with equiaxed grains. Here, we show the strong correlations between the microstructure and magnetic properties and provide insights for the future development of high-performance $SmCo_4B$-based magnets.

Nd-Fe-B and Sm-Co rare-earth permanent magnetic materials exhibit excellent magnetic properties that have led to their widespread use in medical devices, aerospace industry, instrumentation, and hybrid vehicles[1–4]. Commercial $SmCo_5$ sintered permanent magnets exhibit a coercivity of 1.19–1.67 MA·m^{-1} and magnetic energy product ($(BH)_{max}$) of 120–200 kJ·m^{-3} [5–7]. Moreover, $SmCo_5$ is an ideal hard magnetic phase for dual-phase exchange coupled magnets due to its high uniaxial magnetocrystalline anisotropy constant (K_1 ~ 17.2 MJ·m^{-3}) and anisotropic field (H_a ~ 27.85 MA·m^{-1})[8,9]. In addition, the $(BH)_{max}$ of commercial Nd-Fe-B magnets has reached 474 kJ·m^{-3}, nearly 93% of the theoretical limit (512 kJ·m^{-3})[10,11], with only limited improvements in their performance achieved in recent work. Therefore, it is vital to develop ideal hard magnetic phases and fourth-generation rare earth permanent magnets.

$Sm_{1+n}Co_{5+3n}B_{2n}$ compounds have attracted attention due to their high magnetocrystalline anisotropy. The H_a (95.49 MA·m^{-1}) of the $SmCo_4B$ phase with a $CeCo_4B$-type hexagonal structure, estimated via the magnetization curve intersection method, is much greater than that of the $SmCo_5$ phase ($H_a = 56.50$ MA·m^{-1}) at 4.2 K. However, its low saturation magnetization (M_s) and low actual coercivity (H_c) severely restrict possible applications[12–16]. H_c and remanence are related to the intrinsic parameters of the materials (e.g., H_a, Curie temperature (T_C)) and the microstructure. Among these factors, the alloy composition has a significantly greater effect on the magnetic properties than the microstructural parameters (e.g., grain size and orientation). Therefore, optimization of the alloy composition is a common and effective method for improving H_c and M_s by changing the microstructure and intrinsic parameters of the alloy. Substitution of Co with Fe, which has a lower cost and higher magnetic moment[17,18], is a common approach. Jiang et al.[19,20] prepared $SmCo_{4-x}Fe_xB$ ribbons and reported that the $SmCo_3FeB$ alloy composed of a hexagonal $Sm(Co, Fe)_4B$ phase exhibited a high H_c of 3.26 MA·m^{-1} and remanence (M_r) of 29 A · m^2·kg^{-1}, while the $SmCo_2Fe_2B$ alloy composed of $Sm(Co, Fe)_4B$ and $Sm_2(Co, Fe)_{17}B_y$ phases showed an H_c of 2.39 MA·m^{-1} and M_r of 36 A · m^2·kg^{-1}. Satio et al.[21] melt-spun $SmCo_{4-x}Fe_xB$ ribbons at a speed of 50 m · s^{-1} and then annealed them at 700 °C for 1 h. Only $SmCo_4B$ or $Sm(Co, Fe)_4B$ single phases were obtained for $x \le 1.5$, and a maximum H_c of ~1.99 MA·m^{-1} and M_r of 34 A · m^2·kg^{-1} were obtained at $x = 1.5$. Our previous

[1]Hebei Key Laboratory of New Functional Materials, School of Materials Science and Engineering, Hebei University of Technology, Beichen District, Tianjin, China. [2]Songshan Lake Materials Laboratory, Dongguan, China. [3]Beijing National State Key Laboratory of Magnetism, Institute of Physics, Chinese Academy of Sciences, Beijing, China. [4]School of Materials Science and Engineering, Shanghai University, Shanghai, China. ✉e-mail: hbgdsjb@hebut.edu.cn; chixiang@sslab.org.cn; zhangy@iphy.ac.cn; liujian@shu.edu.cn

work[22–24] revealed that $SmCo_4B$-based alloys exhibit a complex $Sm_{1+n}Co_{5+3n}B_{2n}$ multiphase structure. The H_c of the annealed $SmCo_{2.94}FeCu_{0.06}B$ ribbons reached 3.99 MA·m^{-1}, while the M_r was only 27.8 A · m^2·kg^{-1}. The high content of Fe (11.7–33.3 at%)[19,21,22] prevents the alloy from maintaining a stable $SmCo_4B$ main phase and high coercivity, so that the H_c and M_s of the $Sm(Co, Fe)_4B$-based alloy are still not ideal.

Based on first-principles calculations, Söderlind et al.[25,26] found that the replacement of Co with Fe in $SmCo_5$ magnets and the use of Ni as a thermodynamic stabilizer can stabilize the crystal structure of $Sm(Co, Fe)_5$. The calculated $(BH)_{max}$ of the $SmCoNiFe_3$ alloy reached 361 kJ·m^{-3}, which is 56% higher than the experimental value of the $SmCo_5$ magnet (231 kJ·m^{-3})[27]. They also reported that increasing the number of 3 d electrons (particularly due to the addition of Ni atoms) could stabilize the hexagonal $SmTM_5$ compounds (TM = Fe, Co, or Ni). Moreover, the partial substitution of Fe by Ni atoms with a ratio of 3:1 provides additional electron doping. Gavrikov et al.[28] found that increased doping Fe and Ni in $Sm(Co_{1-x-y}Fe_xNi_yB)_5$ (x = 0.15, 0.3, 0.45; y = 0.05, 0.1, 0.15) alloys increased M_s and M_r but decreased H_c. Compared to $SmCo_5$ ribbons melt-spun at 42 m · s^{-1} (H_c = 0.80 MA·m^{-1}), the $Sm(Co_{0.8}Fe_{0.15}Ni_{0.05})_5$ ribbons demonstrate superior magnetic properties, with H_c = 1.03 MA·m^{-1} and M_r = 45 A · m^2·kg^{-1}.

Here, inspired by these previous works[22,25,26,28], we focus on the effect of the Fe and Ni codoping of $SmCo_4B$ compounds. Multiphase $SmCo_{4-x-y}Fe_xNi_yB$ ribbons with platelet-shaped microstructure show a record H_c of up to 6.71 MA·m^{-1}, which is far higher than the H_c of all hard magnetic ribbons. Four microstructures of multicomponent and multihard magnetic phases with ultrahigh room temperature coercivity are synthesized, and their formation mechanisms and impact on magnetic properties are analyzed in detail.

Results and discussion

Phase identification

We designed nine alloys, and their composition ranges and relative relationships are shown in Fig. S1 (Supplementary Fig. S1). Figure 1 shows the XRD patterns of $SmCo_{4-x-y}Fe_xNi_yB$ (Fe_xNi_y, x = 1.0–2.0; y = 0–1.0) as-spun and annealed ribbons. The strong diffraction peaks in all as-spun ribbons correspond to the Sm-Co-B phases (Fig. 1a), where the main phase is $Sm(Co, Fe, Ni)_4B$ (1:4:1), with possible $Sm_5(Co, Fe, Ni)_{19}B_6$ (5:19:6) and/or $Sm_3(Co, Fe, Ni)_{11}B_4$ (3:11:4) phase.

The distinct hump-like and strong diffuse scattering peaks imply a high amorphous content in all of the as-spun ribbons. The amorphous content reaches 91.7 vol% in x = 1.0 and y = 0 ribbons (Fig. 1c). The amorphous content decreases monotonically as the Ni content (y) increases from 0 to 1.0. For the x = 1.2 ribbons, the content of the crystalline phases increases as y increases from 0.4 to 0.8. That is, adding Ni with y < 1.0 improves the stability of the Sm-Co-B phases when x = 1.0–1.2. For the y = 0.8 ribbons, the amorphous content increases as x increases from 1.2 to 1.6, which means that increasing Fe decreases the crystallization of the Sm-Co-B phases. The amorphous content increases monotonically when the Fe and Ni contents increase proportionally (e.g., $Fe_{1.2}Ni_{0.6}$ and $Fe_{2.0}Ni_{1.0}$). A high amorphous content is maintained in the $Fe_{1.0}Ni_0$, $Fe_{1.2}Ni_{0.4}$, $Fe_{1.6}Ni_{0.8}$, and $Fe_{2.0}Ni_{1.0}$ ribbons as the Fe and Ni contents increase simultaneously, implying that adding Ni to x > 1.0 ribbons cannot suppress the trend of decreasing the crystallization of the Sm-Co-B phases caused by increasing Fe content. Therefore, increasing the Fe content helps to increase the glass-forming ability (GFA) and reduce the crystallization of the 1:4:1 phase in the as-spun ribbons. For x = 1.0–1.2, increasing the Ni content promoted the crystallization of the Sm-Co-B phases.

Figure 1b shows the XRD patterns and refinement results for Fe_xNi_y ribbons annealed at 850 °C for 30 min, with the corresponding Rietveld refinement results provided in Table S1 (Supplementary Table S1). The relative content of each phase is shown in Fig. 1d. The phase content is related to the total Fe + Ni content, i.e., it depends mainly on the Co content. As the Fe + Ni content ($x + y$) increases from 1.0 (alloy 1) to 2.0 (alloy 6), i.e., as the Co content decreases, the 1:4:1 content monotonically decreases, and the 3:11:4 content monotonically increases. However, for $2.0 \le x + y \le 3.0$ and $0.8 \le y \le 1.0$, the increase in the Fe content reduces the amount of the 3:11:4 phase and increases the amount of the 1:4:1 and 1.1:4:4:4 phases.

Ignoring the contents of the 2:7:3, 2:14:1, and 1.1:4:4 phases, the relative contents of the main 1:4:1, 5:19:6, and 3:11:4 phases are compared in Fig. S2a. Alloys with x = 1.2, y = 0.4–0.8, and $x + y \le 2.0$ tend to form the 3:11:4 phase, and alloys with y = 1.0 and $x + y > 2.0$ tend to form the 1:4:1 phase. For the x = 1.0 and y = 0–0.4 ribbons, increasing the Ni content improved the structural stability of the 3:11:4 phase. According to the Sm-Co-B diagram in Fig. S2b, the 1:4:1, 5:19:6, 3:11:4, and 2:7:3 phases have the same Sm content, whereas the B content increases and the Co content decreases. The formation energies of the pure $SmCo_4B$, $Sm_3Co_{11}B_4$, and $Sm_2Co_7B_3$ phases are −0.252, −0.312, and −0.318 eV/atom, respectively[29], which are stable phases. For the nine alloys with a nominal composition of $Sm(Co, Fe, Ni)_4B$, the main phases are 1:4:1, 5:19:6, and 3:11:4. However, the addition of different contents of Fe and Ni changes the composition of the alloy's phase transformation (Fig. S2b).

Therefore, the formation mechanisms of the 1:4:1, 5:19:6, 3:11:4, and 2:7:3 phases proceed as follows: (1) During the melt-spinning process, the ribbons form the same microstructure of Sm-Co-B nanocrystalline phases embedded in the amorphous matrix. During the subsequent annealing process, two processes occur simultaneously: small-grain growth and crystallization of the amorphous phase. (2) The addition of Fe and Ni changes the phase transition point of the crystallization of the amorphous phase, leading to changes in the phase composition and relative phase content. (3) Most crystalline Sm-Co-B phases are formed through the crystallization of the amorphous matrix.

Dynamics of phase transformation

We investigated the phase transition during the crystallization process of the amorphous phase in the as-spun $Fe_{1.0}Ni_{1.0}$ and $Fe_{2.0}Ni_{1.0}$ ribbons due to their lowest and highest amorphous content, respectively. Figures S2 and S4 show the XRD patterns and refinement results of the $Fe_{1.0}Ni_{1.0}$ and $Fe_{2.0}Ni_{1.0}$ ribbons after annealing at different temperatures for 30 min, and the corresponding structural parameters are listed in Tables S2 and S3, respectively. Figure 2 shows the relationship between the temperature and phase fraction of the annealed $Fe_{1.0}Ni_{1.0}$ and $Fe_{2.0}Ni_{1.0}$ ribbons. As the annealing temperature increases, the high Fe content (x = 2.0) promotes the formation of a high content of the 1:4:1 phase in the ribbons, while the amounts of the 2:7:3, 3:11:4 and 5:19:6 phases decreased, indicating that the high Fe content in the ribbons improved the structural stability of the 1:4:1 phase at high temperatures and reduced the stability of the 2:7:3, 3:11:4, and 5:19:6 phases. Additionally, in the ribbons with low Fe content (x = 1.0), the relative contents of the 1:4:1, 2:7:3, 3:11:4, and 5:19:6 phases remained unchanged, indicating that their phase content reached equilibrium. The phase equilibrium is achieved because the Fe content in each phase is not high, and the annealing temperature is only an external factor that affects the phase stability. Thus, the dissolved Fe content is the main factor determining the structural stability of the 1:4:1, 2:7:3, 3:11:4, and 5:19:6 phases. Moreover, a high Fe content and high annealing temperature are more favorable for the formation of the 1.1:4:4 and 2:14:1 phases, and the annealing temperature required for the formation of the 1.1:4:4 and 2:14:1 phases decreases with higher Fe content.

Moreover, the multiple exothermic peaks in the differential scanning calorimetry (DSC) curves of the Fe_xNi_y ribbons in Fig. S5 confirm the segmented crystallization behavior of the ribbons. Based on the XRD patterns, the stepwise crystallization process of Fe_xNi_y

https://doi.org/10.1038/s41467-024-54610-6

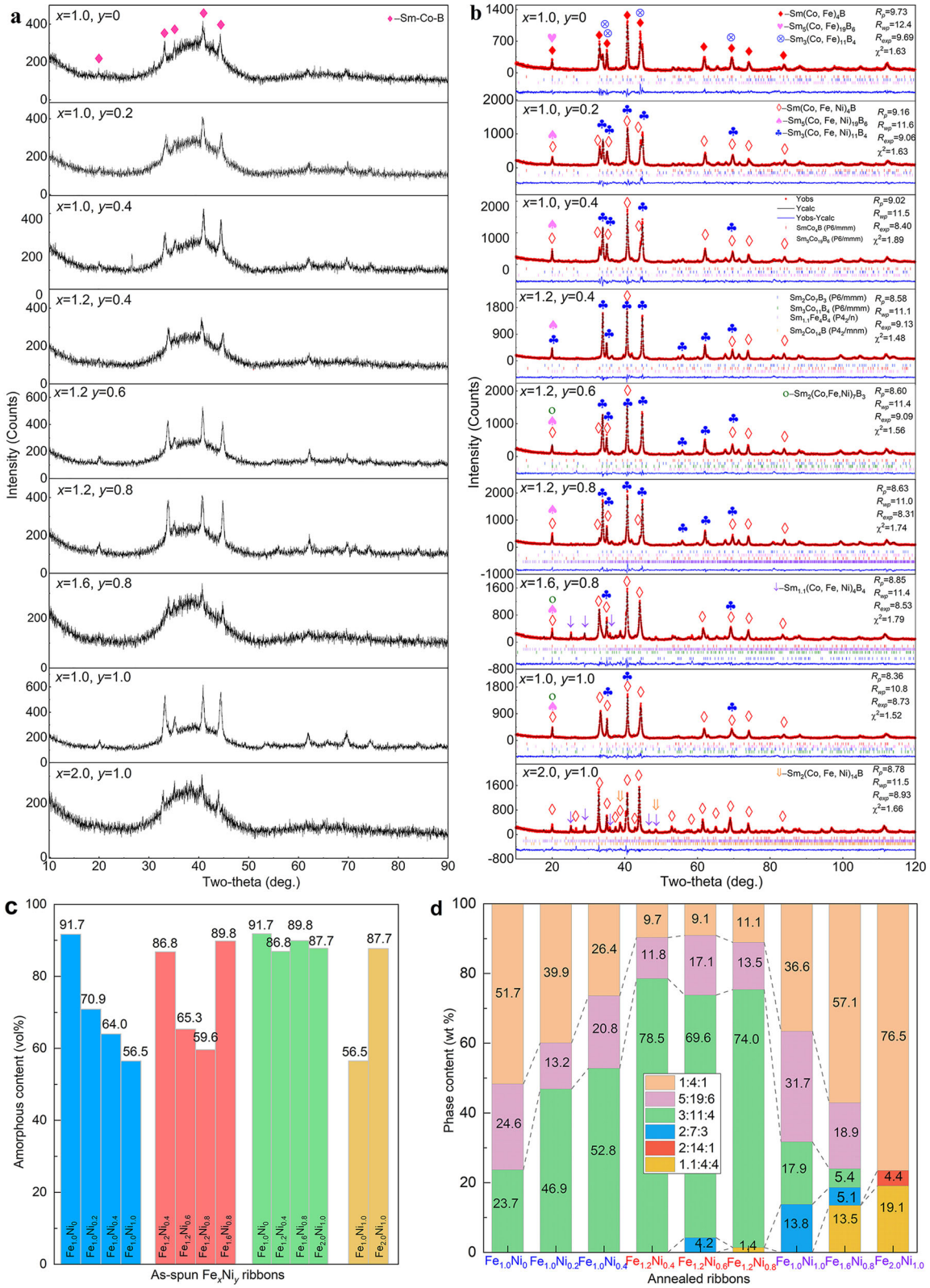

Fig. 1 | XRD patterns of the $SmCo_{4-x-y}Fe_xNi_yB$ ($x = 1.0–2.0$; $y = 0–1.0$) ribbons. a As-spun ribbons. **b** Ribbons annealed at 850 °C for 30 min. **c** Amorphous phase percentage in the as-spun ribbons. **d** Phase percentages in the annealed ribbons.

ribbons can be summarized as: [Initial state: as-spun ribbons → amorphous + Sm-Co-B phases below 500 °C] →[First stage crystallization: amorphous → (1:4:1 + 5:19:6) + 3:11:4 + 2:7:3 at 525–573 °C] → [Second stage crystallization: amorphous → (1:4:1 + 5:19:6) + 3:11:4 + 2:7:3 + 2:14:1 + 1.1:4:4 at 600–865 °C] →[Third stage phase transition: 5:19:6 + 3:11:4 + 2:7:3 → 1:4:1 + 2:14:1 + 1.1:4:4 or 5:19:6 + 3:11:4 + 2:7:3 → 1:4:1 + 5:19:6 + 3:11:4 + 2:7:3 + 2:14:1 above 850 °C].

Melt spinning is a far-from-equilibrium process that is dominated by kinetics. Due to the nonequilibrium kinetics of melt-spinning, the $SmCo_{4-x-y}Fe_xNi_yB$ ribbons are composed of different phases.

https://doi.org/10.1038/s41467-024-54610-6

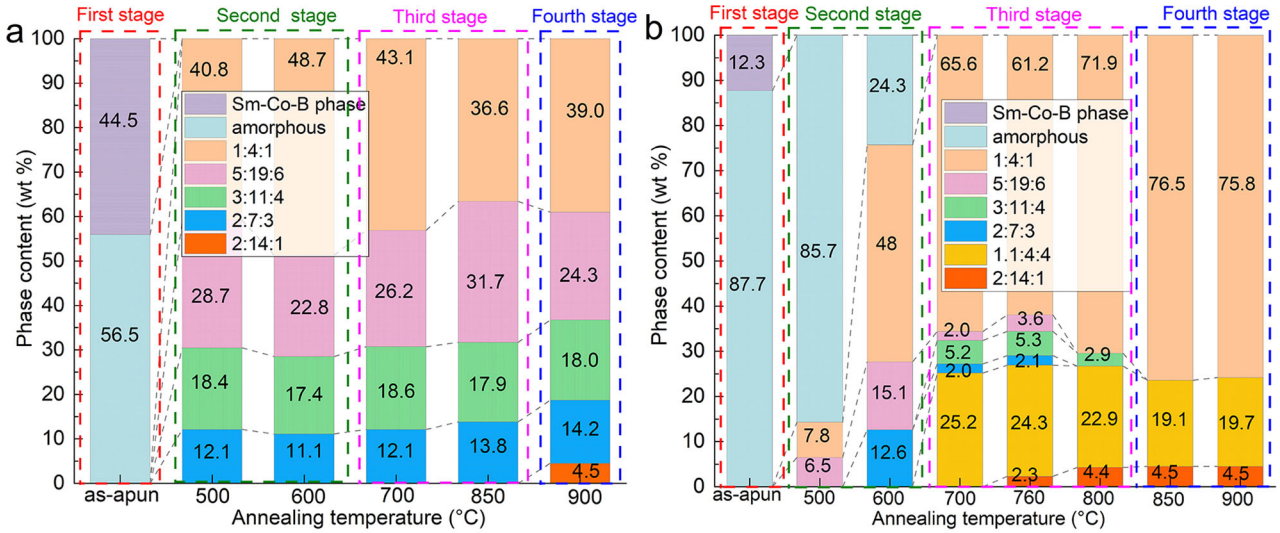

Fig. 2 | Relationship between the temperature and phase fraction of the annealed ribbons. a $Fe_{1.0}Ni_{1.0}$. **b** $Fe_{2.0}Ni_{1.0}$.

Moreover, nonequilibrium crystallization leads to metastable phases and changes in the phase content, which can be explained by the formation energy of the phases. For the Nd-Co-B system, as the Co content decreases and the B content increases, the phase formation energy (E) in the Materials Project database[29] decreases in the order of $E_{Nd2Co14B}$ (−0.119 eV/atom) > E_{NdCo4B} (−0.216 eV/atom) > $E_{Nd5Co19B6}$ (−0.253 eV/atom) > $E_{Nd3Co11B4}$ (−0.278 eV/atom) > $E_{Nd2Co7B3}$ (−0.305 eV/atom) > $E_{NdCo4B4}$ (−0.462 eV/atom). Similarly, for the Sm-Co-B system, $E_{Sm2Co14B}$ (−0.141 eV/atom) > E_{SmCo4B} (−0.252 eV/atom) > $E_{Sm3Co11B4}$ (−0.312 eV/atom) > $E_{Sm2Co7B3}$ (−0.337 eV/atom) > $E_{Sm1.1Co4B4}$ (−0.475 eV/atom). Therefore, high temperatures (> 760 °C) favor the formation of the $Sm_2Co_{14}B$ phase. Additionally, the composition of the alloy is close to that of $SmCo_4B$ (Fig. S2b), hindering the formation of the 1.1:4:4 phase in the as-spun ribbons. However, this phase can precipitate from the amorphous matrix due to its minimum formation energy, so the 25.2 wt% 1.1:4:4 phase is formed in the $Fe_{2.0}Ni_{1.0}$ ribbons annealed at 700 °C. For the Sm-M system, E_{SmFe5} (0.00650 eV/atom) > E_{SmCo5} (−0.0662 eV/atom) > E_{SmNi5} (−0.299 eV/atom)[29]. Correspondingly, E_{SmFe4B} > E_{SmCo4B} (−0.252 eV/atom) > E_{SmNi4B} (−0.451 eV/atom). Therefore, after the addition of Fe, Ni plays an essential role in obtaining the 1:4:1, 5:19:6, 3:11:4, and 2:7:3 phases with the same P6/mmm space group, and the relative contents of Fe and Ni are critical.

Microstructure

Figure 3 shows TEM images of Fe_xNi_y (x = 1.0–1.6; y = 0–0.8) ribbons annealed at 850 °C for 30 min and EDS mapping images of the $Fe_{1.6}Ni_{0.8}$ ribbon before and after annealing at 850 °C for 30 min. Annealed $Fe_{1.0}Ni_0$ ribbons are composed of equiaxed grains with sizes in the 62.5–184.6 nm range (Fig. 3a). The fast Fourier transform (FFT) patterns (Fig. S6a_2 – a_3) confirm that the annealed $Fe_{1.0}Ni_0$ ribbon consists of 1:4:1, 5:19:6, and 3:11:4 grains. The annealed $Fe_{1.0}Ni_{0.2}$ ribbon (Fig. 3b) consists of equiaxed grains with sizes in the 59.7–157.9 nm range. The selected area electron diffraction (SAED) patterns (Fig. S6b_1 – b_3) confirm that the annealed $Fe_{1.0}Ni_{0.2}$ ribbon consists of 1:4:1, 5:19:6, and 3:11:4 grains. The annealed $Fe_{1.0}Ni_{0.4}$ ribbon (Fig. 3c) consists of equiaxed grains with sizes in the 51.4–150.7 nm range, which are slightly smaller than those in Fig. 3a, b. The inset FFT patterns (Fig. S6c_1) show that the equiaxed grains are in the 1:4:1 and 3:11:4 phases. The FFT pattern (Fig. S6c_3) shows that the ribbon consists of 1:4:1, 5:19:6, and 3:11:4 grains and that the grains are in direct contact with each other and do not show a specific orientation relationship.

The annealed $Fe_{1.2}Ni_{0.4}$ ribbon (Fig. 3d) consists of equiaxed grains with sizes in the 56.1–200.1 nm range. The FFT patterns (Fig. S6d_1 – d_3) show that the ribbon consists of 1:4:1, 5:19:6, and 3:11:4 grains. When y increases to 0.6, the grain size and phase distribution are similar to those of the ribbons with y = 0.4. As shown in Fig. 3e, f, the $Fe_{1.2}Ni_{0.6}$ ribbon consists of the 1:4:1, 3:11:4, 5:19:6, and 2:7:3 grains. The grain sizes of the annealed $Fe_{1.2}Ni_{0.8}$ ribbon are in the 79.5–202.3 nm range, as shown in Fig. 3g. The FFT patterns (Fig. S6f_1–f_3) show that the equiaxed grains are 1:4:1, 3:11:4, 5:19:6, and 1.1:4:4 phases. The as-spun $Fe_{1.6}Ni_{0.8}$ ribbon (Fig. 3h) is composed of poorly crystallized 1:4:1 nanograins with the sizes in the 10–30 nm range distributed on the amorphous matrix (Fig. S7). The high-angle annular dark-field (HAADF) image and the map scanning images in Fig. 3k indicate that Sm, Co, Fe, Ni, and B are distributed uniformly, with no component segregation or crystalline phases. The energy dispersive spectroscopy (EDS) results show that the as-spun $Fe_{1.6}Ni_{0.8}$ ribbon mainly consists of the 1:4:1 phase with a Sm:(Fe, Co, Ni) ratio of 1:4.3.

The SEM image in Fig. 3i shows that the annealed $Fe_{1.6}Ni_{0.8}$ ribbon consists of platelet-shaped and equiaxed grains with two different sizes. The long platelet-shaped grains, marked in red with the lengths of 1.5–4.0 μm and widths of 0.2–0.6 μm, are the first phase to form. The short grains, marked in blue, are 0.5–1.2 μm long and 0.1–0.4 μm wide. The short platelet-shaped grains are distributed between long grains and are the phases formed after the long grains. The average size of the equiaxed grains is approximately 1.0 μm, as indicated by the white arrow, and these grains may precipitate after the long platelet-shaped grains and short platelet-shaped grains. Table 1 shows the EDS results for positions 1–7 in Fig. 3i, l. The equiaxed grains at position 1 and the long platelet-shaped grains at position 2 are $Sm_{8.92}Co_{13.09}Fe_{17.81}Ni_{2.98}B_{57.20} = Sm_{1.0}(Co_{0.39}Fe_{0.53}Ni_{0.09})_{3.80}B_{6.41}$ and $Sm_{9.52}Co_{16.22}Fe_{11.53}Ni_{8.34}B_{54.39} = Sm_{1.0}(Co_{0.45}Fe_{0.32}Ni_{0.23})_{3.79}B_{5.71}$, respectively, which are close to Sm:(Co+Fe+Ni) = 1:3.8. Moreover, the equiaxed grains are rich in Fe-B and poor in Co-Ni, whereas the platelet-shaped grains are rich in Co-Ni and poor in B, indicating that the equiaxed grains may be a slightly B-rich 5:19:6 phase and that the platelet-shaped grains are the 1:4:1 phase. In other words, the addition of Ni promotes the formation of platelet-shaped grains.

The TEM images in Fig. 3j show that the annealed $Fe_{1.6}Ni_{0.8}$ ribbon consists of platelet-shaped grains with three different sizes. The largest grains correspond to the grains marked in red in Fig. 3i; the medium-sized grains are 560.3–1146.9 nm long and 118.3–215.3 nm wide and are marked in blue, which is consistent with the blue marked grains in Fig. 3i. The smallest ones are 132.3–348.7 nm long and 69.8–124.1 nm wide, marked in green. Nevertheless, the grain size is too small for

https://doi.org/10.1038/s41467-024-54610-6

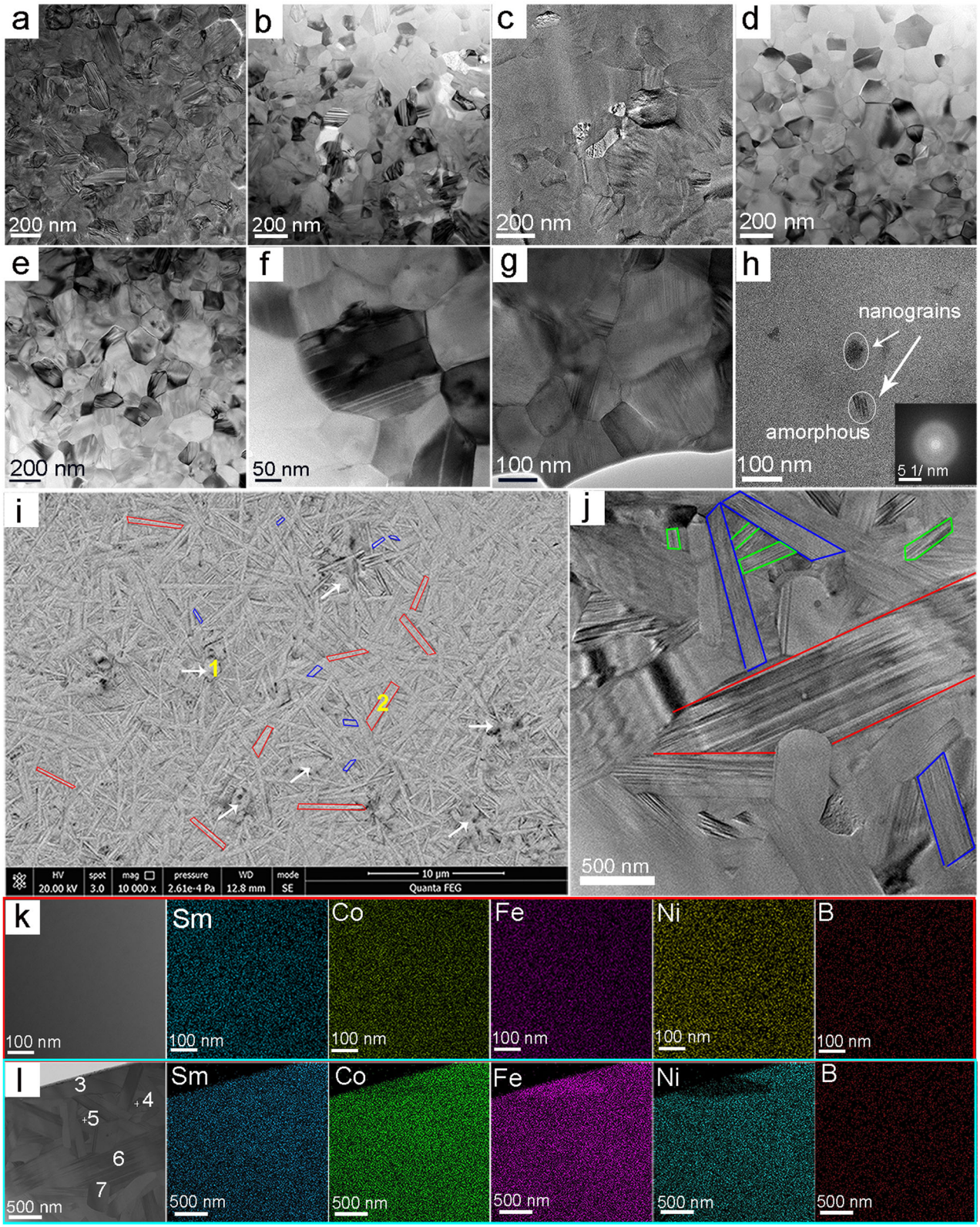

Fig. 3 | Microstructures of Fe_xNi_y ribbons annealed at 850 °C for 30 min and EDS mapping images of the $Fe_{1.6}Ni_{0.8}$ ribbon before and after annealing at 850 °C for 30 min. a TEM image of the annealed $Fe_{1.0}Ni_0$ ribbon. **b** TEM image of the annealed $Fe_{1.0}Ni_{0.2}$ ribbon. **c** TEM image of the annealed $Fe_{1.0}Ni_{0.4}$ ribbon. **d** TEM image of the annealed $Fe_{1.2}Ni_{0.4}$ ribbon. **e**, **f** TEM images of the annealed $Fe_{1.2}Ni_{0.6}$ ribbon. **g** TEM image of the annealed $Fe_{1.2}Ni_{0.8}$ ribbon. **h** TEM image of the as-spun $Fe_{1.6}Ni_{0.8}$ ribbon. **i** SEM image of the annealed $Fe_{1.6}Ni_{0.8}$ ribbon. **j** TEM image of the annealed $Fe_{1.6}Ni_{0.8}$ ribbon. HAADF and EDS mapping images of as-spun (**k**) and annealed (**l**) $Fe_{1.6}Ni_{0.8}$ ribbons.

Table 1 | EDS results (at%) corresponding to Fig. 3i, l

Position	Sm	Co	Fe	Ni	B	Chemical components
1	8.92	13.09	17.81	2.98	57.20	$Sm_{1.0}(Co_{0.386}Fe_{0.526}Ni_{0.088})_{3.798}B_{6.413}$
2	9.52	16.22	11.53	8.34	54.39	$Sm_{1.0}(Co_{0.449}Fe_{0.319}Ni_{0.231})_{3.791}B_{5.713}$
3	12.49	16.37	30.15	0.73	40.26	$Sm_{1.0}(Co_{0.346}Fe_{0.638}Ni_{0.015})_{3.783}B_{3.223}$
4	16.05	29.61	18.55	12.41	23.38	$Sm_{1.0}(Co_{0.489}Fe_{0.306}Ni_{0.205})_{3.774}B_{1.457}$
5	16.74	32.62	21.87	15.36	13.41	$Sm_{1.0}(Co_{0.467}Fe_{0.313}Ni_{0.220})_{4.173}B_{0.801}$
6	18.36	33.28	25.49	18.04	4.83	$Sm_{1.0}(Co_{0.433}Fe_{0.332}Ni_{0.235})_{4.184}B_{0.236}$
7	16.92	28.27	23.24	15.91	15.66	$Sm_{1.0}(Co_{0.419}Fe_{0.345}Ni_{0.236})_{3.985}B_{0.926}$

these grains to be observed in Fig. 3i. The grains with different sizes are arranged randomly. The FFT pattern presented in Fig. S7g shows that the small platelet-shaped grains consist of the 3:11:4, 1:4:1, and 2:7:3 phases. The FFT pattern presented in Fig. S7i shows that the ribbon is composed of long platelet-shaped 1.1:4:4 grains and short platelet-shaped 5:19:6 grains.

Combined with the FFT patterns in Fig. S7g, i, the grain at position 3 in Fig. 3l can be identified as the 1.1:4:4 phase, which is rich in Fe and poor in Co-Ni. The grain at position 4 is the 2:7:3 phase, which is poor in Fe and rich in Co-Ni. The grains at positions 5 and 6 both correspond to the 1:4:1 phase. The grain at position 7 is the 5:19:6 phase, which is poor in Fe and rich in Co-Ni. Moreover, Sm, Co, Fe, Ni, and B still have homogeneous distributions, as shown in the EDS mapping images in Fig. 3l.

The as-spun $Fe_{1.6}Ni_{0.8}$ ribbons consist of 89.8 vol% amorphous matrix and 10.2 vol% Sm-Co-B nanograins. During annealing, the longest platelet-shaped 1:4:1 grains are formed first, followed by the short grains, and finally, the smallest 2:7:3 grains are formed. The $Sm_{1.1}Co_4B_4$ phase is rich in Fe and poor in Co-Ni, indicating that the likelihood of the formation of the 1.1:4:4 phase increases with higher Fe content, which leads to the formation of the ~20 wt% 1.1:4:4 phase in the $Fe_{2.0}Ni_{1.0}$ ribbons annealed at 700–900 °C, as shown in Fig. S4. Because more Fe atoms are dissolved into the 1.1:4:4 phase, the matrix becomes poor in Fe and rich in Co-Ni. This results in the formation of a higher content of the Sm(Co, Ni)$_4$B phase due to the reduced formation energy of dissolved Ni (E_{SmCo4B} (−0.252 eV/atom) > $E_{SmCo3NiB}$ (−0.286 eV/atom)> E_{SmNi4B} (−0.451 eV/atom))[29]. In addition, Table S1 also shows the presence of 5.4 wt% 3:11:4 phase in the annealed $Fe_{1.6}Ni_{0.8}$ ribbons, most likely in the form of platelet-shaped grains, which are not observed in Fig. 3j.

Figure 4a shows that the annealed $Fe_{1.0}Ni_{1.0}$ ribbon consists of platelet-shaped grains with two different sizes and equiaxed grains with an average width of 248.2 nm. The long platelet-shaped grains are 0.5–1.4 μm long and 156.6–408.3 nm wide, and the short grains are 137.1–380.2 nm long and 60.2–190.4 nm wide. Figure 4b, c shows the HRTEM images of regions A and B in Fig. 4a, respectively. The corresponding FFT patterns (Fig. S8a_2 – a_3 and a_5) demonstrate that the platelet-shaped grains in region A are the 3:11:4 and 5:19:6 phases, and those in region B are the 1:4:1, 2:7:3, and 5:19:6 phases. Figure 4d presents an enlarged view of region C in Fig. 4a, and the FFT patterns in Fig. S8a_7 show that the equiaxed grains are in the 1:4:1, 2:7:3, and 5:19:6 phases. Based on the relative positions of the grains, it can be inferred that the long platelet-shaped grains formed first, followed by short platelet-shaped grains, and then equiaxed grains.

Figure 4e shows an SEM image of the annealed $Fe_{2.0}Ni_{1.0}$ ribbon. The ribbon is composed of platelet-shaped grains and blocky grains. The platelet-shaped grains are 1.0–5.0 μm long and 150.2–570.5 nm wide, and the blocky grains are 190.5–430.8 nm long. The grains at positions 1 and 2 are $Sm_{9.45}Co_{9.91}Fe_{17.77}Ni_{8.98}B_{53.89}$ = $Sm_{1.0}(Co_{0.270}Fe_{0.485}Ni_{0.245})_{3.879}B_{5.70}$ and $Sm_{9.20}Co_{10.21}Fe_{15.81}Ni_{9.07}B_{55.71}$ = $Sm_{1.0}(Co_{0.291}Fe_{0.451}Ni_{0.258})_{3.814}B_{6.06}$, respectively, both of which are the 1:4:1 main phase according to the XRD pattern in Fig. 1b. However, the blocky grain at position 1 is slightly rich in Fe. By contrast, the platelet-shaped grain at position 2 is somewhat rich in Co-Ni, indicating that blocky and platelet-shaped grains correspond to different stages of crystallization. Figure 4f shows the staggered distribution of platelet-shaped and equiaxed grains in the annealed $Fe_{2.0}Ni_{1.0}$ ribbon. The equiaxed grains sizes are in the 178.6–370.8 nm range, corresponding to the blocky grains in Fig. 4e. The SAED patterns in Fig. S8b_2 – b_3 prove that the grains at positions D and E are the 1.1:4:4 and 1:4:1 phases, respectively. Figure 4h shows an enlarged view of the location in Fig. 4g. The corresponding FFT patterns in Fig. S8b_6 – b_8 prove that the circular grain (position F) is a paramagnetic[30] 1.1:4:4 grain, and the surrounding grains (positions G and H) are hard magnetic 1:4:1 and 2:14:1 phases. These results indicate that during heating to 850 °C, the formation of the 2:7:3, 5:19:6, and 3:11:4 phases is suppressed. Therefore, the amorphous phase mainly undergoes phase transformation through the following pathways: the amorphous phase continuously crystallizes into platelet-shaped 1:4:1 grains when the temperature is higher than ~500 °C, followed by crystallization of the amorphous phase into equiaxed 1:4:1 grains between the platelet-shaped 1:4:1 grains above 700 °C. Finally, the residual amorphous phase transforms into spherical 1.1:4:4 grains accompanied by the formation of 2:14:1 grains in the surrounding Co-rich areas.

In summary, the as-spun Fe_xNi_y ribbons consisted of an amorphous matrix and a small amount of Sm-Co-B nanocrystalline phases. Fe addition enhances the formation of the amorphous phase of the as-spun ribbons, while Ni addition has the opposite effect. During subsequent annealing, the amorphous phase crystallizes in stages. The addition of Fe or Ni changes the phase composition, shape, and size of the grains. For $x < 1.6$ and $y < 0.8$, the grains in the annealed Fe_xNi_y ribbons are all equiaxed, whereas the grains are platelet shaped for $y > 0.8$, and the platelet-shaped grains are similar to those in the hot-deformed Nd-Fe-B or Sm-Co magnets[9,31,32]. However, the different platelet-shaped grains are randomly oriented. Therefore, if stress is applied, these platelet-shaped grains may be aligned, which may be beneficial for the preparation of hot-deformed magnets.

$SmCo_4B$ (m = 1, n = 1), $Sm_5Co_{19}B_6$ (m = 2, n = 3), $Sm_3Co_{11}B_4$ (m = 1, n = 2), and $Sm_2Co_7B_3$ (m = 1, n = 3) structures are formed by alternate stacking of m layers of $CaCu_5$-type $SmCo_5$ and n layers of $CeCo_3B_2$-type $SmCo_3B_2$ along the *c*-axis[33]. Their crystal structures have strong uniaxial anisotropy, as shown in Fig. S9. Figures S7g, S8a_2 and S8a_5 show an orientation relationship between 3:11:4 and 2:7:3, between 5:19:6 and 2:7:3, between 3:11:4 and 5:19:6, and between 1:4:1 and 2:7:3. Table 1 shows that the Sm:(Co+Fe+Ni) ratios in the 1:4:1, 5:19:6, 3:11:4 and 2:7:3 grains are 1:4.173, 1:3.985, 1:3.783, and 1:3.774, respectively. Therefore, their crystal structure and composition differences are so small that the nucleation and growth of 3:11:4, 5:19:6, and 2:7:3 grains are always accompanied by 1:4:1 grains. Additionally, the orientation relationship between these phases promotes the formation of platelet-shaped grains. However, these platelet-shaped grains differ from those formed by hot deformation. Due to the lack of external pressure applied in this experiment, the growth rate of the grains varies in different directions. The1:4:1, 5:19:6, 3:11:4, and 2:7:3 grains with different sizes compete for growth, and the extrusion between them results in growth along different directions. Therefore, the grains cannot be arranged neatly

https://doi.org/10.1038/s41467-024-54610-6

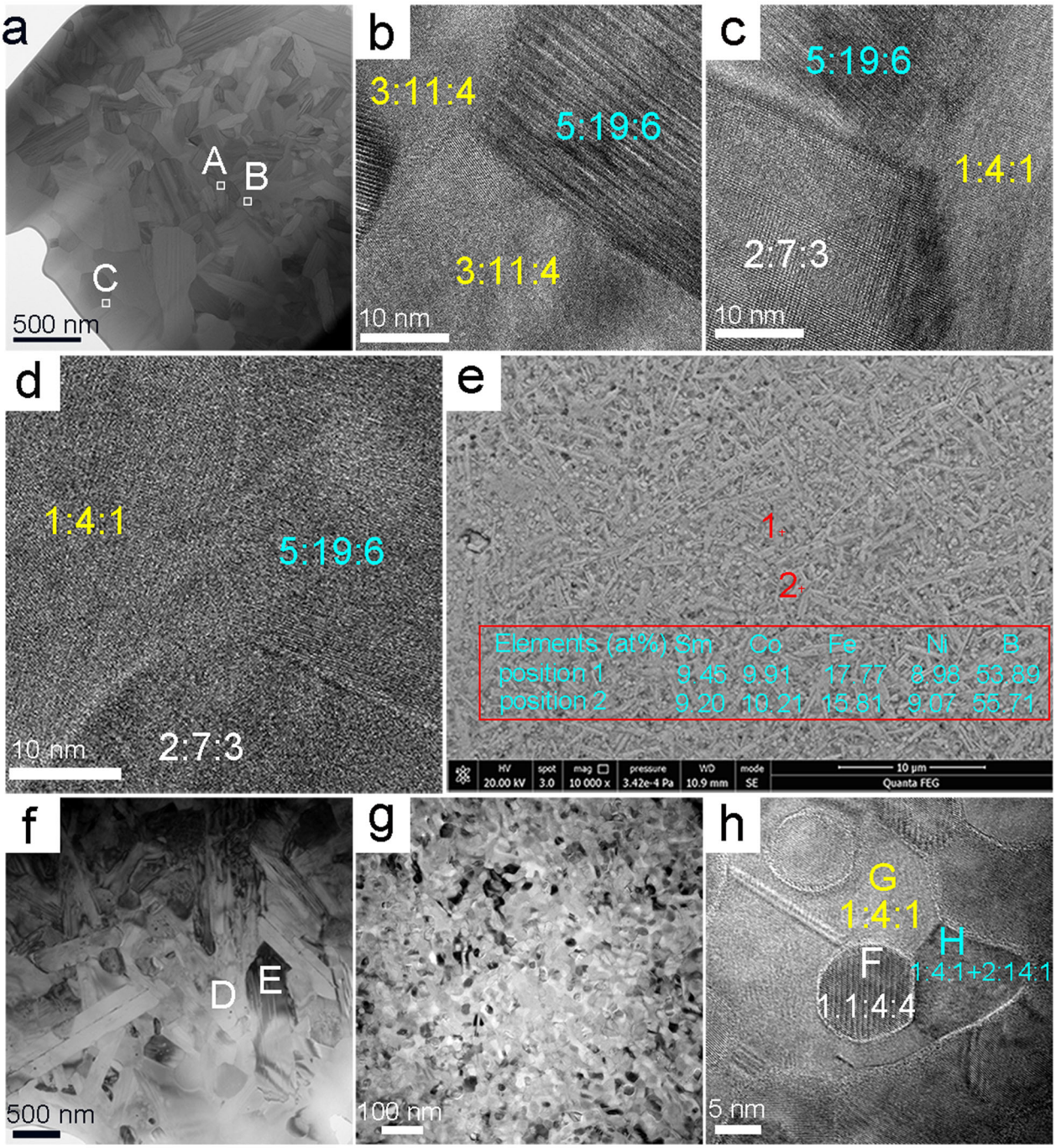

Fig. 4 | Microstructures of the $Fe_{1.0}Ni_{1.0}$ and $Fe_{2.0}Ni_{1.0}$ ribbons annealed at 850 °C for 30 min. a TEM image of the $Fe_{1.0}Ni_{1.0}$ ribbon. **b** HRTEM image of region A in (**a**). **c** HRTEM image of region B in (**a**). **d** HRTEM image of region C in (**a**). **e** SEM image of the $Fe_{2.0}Ni_{1.0}$ ribbon. **f** TEM image of the $Fe_{2.0}Ni_{1.0}$ ribbon. **g** Another TEM image of the $Fe_{2.0}Ni_{1.0}$ ribbon. **h** Enlarged HRTEM image of (**g**).

during annealing; rather, they grow randomly. Our previous research[24] revealed that the long axis orientation of the platelet-shaped 1:4:1 grains tends to be perpendicular to the {100}, {110}, and {112} planes and that the short axes orientate perpendicular to the {116} and {102} planes.

Domain structures

Two ribbons with equal Fe + Ni contents ($x + y = 2.0$) were selected to further understand the relationships between the microstructure, magnetic domains, and magnetic properties. Domain walls are observed as black and white lines in the overfocus and underfocus LTEM images presented in Fig. 5. Magnetic domain walls with widths of 18.3–24.7 nm were observed at the grain junctions of the annealed $Fe_{1.2}Ni_{0.8}$ ribbon, as indicated by the arrows in Fig. 5a, c. The domain walls of the annealed $Fe_{1.0}Ni_{1.0}$ ribbon are located within the platelet-shaped grains with the widths of 13.8–23.5 nm, as indicated by the arrows in Fig. 5d, f, and the domain wall is perpendicular to the longitudinal direction of the stripe within the grain and crosses the entire grain. The critical single-domain radius of a ferromagnet can be calculated according to Eq. (1)[34],

$$R_{sd} \approx 72(AK_1)^{\frac{1}{2}}/\mu_0 M_s^2 \quad (1)$$

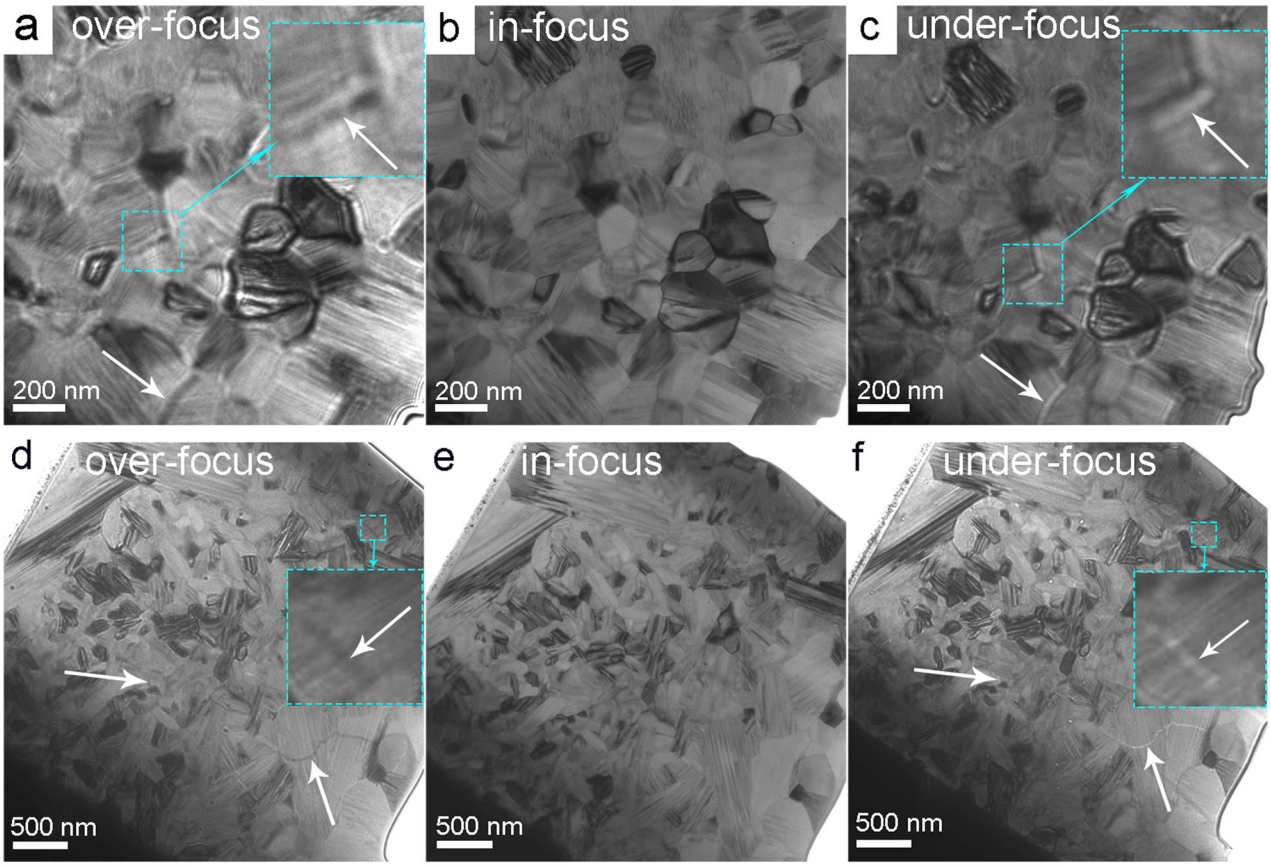

Fig. 5 | LTEM images of the $Fe_{1.2}Ni_{0.8}$ and $Fe_{1.0}Ni_{1.0}$ ribbons annealed at 850 °C for 30 min. a, b, c Overfocus, in-focus, and underfocus images of the $Fe_{1.2}Ni_{0.8}$ ribbon. **d, e, f** Overfocus, in-focus, and underfocus images of the $Fe_{1.0}Ni_{1.0}$ ribbon.

A can be obtained from the domain wall width of $SmCo_4B$ ($\delta = \pi\sqrt{\frac{A}{K}} = 2.8$nm)[19]. If $A = 17$ pJ·m^{-1}, $K_1 = 22.3$ MJ·m^{-3}, and $\mu_0 M_s = 0.46$ T are used for the $SmCo_4B$ phase[35], the corresponding $R_{sd} = 8.2$ μm. Figure 3g shows that the grain size of the annealed $Fe_{1.2}Ni_{0.8}$ ribbons is 79.5–202.3 nm, indicating that all of the grains are single-domain. Moreover, no continuous or closed-loop domain walls are observed in the $Fe_{1.2}Ni_{0.8}$ ribbons. Only some grain boundaries show a contrast similar to that of the magnetic domain walls in Fig. 5a, c, indicating that the domain walls are distributed mainly along the grain boundaries. Therefore, the grain boundaries act as the pinning locations for the movement of magnetic domain walls. By contrast, intermittent domain walls passing through the larger platelet-shaped grains can be directly observed in the annealed $Fe_{1.0}Ni_{1.0}$ ribbon.

The microstructures of the annealed Fe_xNi_y ribbons can be summarized using four models, as shown in Fig. 6. (1) Figure 6a shows that the annealed Fe_xNi_y ($x = 1.0$–1.2; $y = 0$–0.8) ribbons consist of 1:4:1, 3:11:4, and 5:19:6 equiaxed grains with sizes in the 51.4–202.3 nm range. (2) As shown in Fig. 6b, the annealed $Fe_{1.6}Ni_{0.8}$ ribbons consist of platelet-shaped 1:4:1, 3:11:4, 5:19:6, 2:7:3, and 1.1:4:4 grains with three different sizes and a small number of equiaxed 5:19:6 grains with an average size of 1.0 μm. The largest platelet-shaped grains are 1.5–4.0 μm long and 0.2–0.6 μm wide; the medium-sized grains are 0.5–1.2 μm long and 0.1–0.4 μm wide; and the smallest grains are 132.3–348.7 nm long and 69.8–124.1 nm wide and are distributed between the larger platelet-shaped grains. (3) The annealed $Fe_{1.0}Ni_{1.0}$ ribbons contain platelet-shaped and equiaxed 1:4:1, 3:11:4, 5:19:6, and 2:7:3 grains, as shown in Fig. 6c. The long platelet-shaped grains have lengths in the 0.5–1.4 μm range and widths in the 156.6–408.3 nm range, and the short grains have lengths in the 137.1–380.2 nm range and widths in the 60.2–190.4 nm range. The average size of the equiaxed grains is approximately 248.2 nm. (4) Fig. 6d shows that two morphologies coexist in the annealed $Fe_{2.0}Ni_{1.0}$ ribbons. Most of the morphology consists of randomly oriented platelet-shaped 1:4:1 grains with lengths of 1.0–5 μm and widths of 150.2–570.5 nm and equiaxed 1:4:1 and 1.1:4:4 grains with sizes of 190.5–430.8 nm. Additionally, spherical 1.1:4:4 grains with sizes of 5.0–15 nm embedded in small equiaxed 1:4:1 and 2:14:1 grains are present, as shown in Fig. 6e.

Magnetic characterization

Figure 7a, b shows the initial magnetization curves and the corresponding first-order derivative curves of the annealed Fe_xNi_y ribbons obtained from PPMS measurements at 160 kOe (12.73 MA·m^{-1}, Fig. S16 and Table S4). For both annealed $Fe_{1.6}Ni_{0.8}$ and annealed $Fe_{2.0}Ni_{1.0}$ ribbons, the magnetization increases rapidly with increasing applied magnetic field, exhibiting a one-step magnetization process. For the other annealed ribbons, the initial magnetization curves show a two-step magnetization process with two knee points, indicating the existence of a pinning mechanism (Figs. S11–S15). The first nucleation fields are very small, but the second nucleation fields (or pinning fields) of the annealed $Fe_{1.0}Ni_0$, $Fe_{1.0}Ni_{0.2}$, $Fe_{1.0}Ni_{0.4}$, $Fe_{1.2}Ni_{0.4}$, $Fe_{1.2}Ni_{0.6}$, $Fe_{1.2}Ni_{0.8}$, and $Fe_{1.0}Ni_{1.0}$ ribbons are 1.81, 2.24, 2.79, 2.24, 3.18, 3.99, and 6.18 MA·m^{-1}, respectively, increasing monotonically with increasing Ni, Fe, and Fe + Ni contents.

Figure 7c–e shows the hysteresis loops of the annealed ribbons. The corresponding magnetic parameters are listed in Table 2. The hysteresis loops of the $Fe_{1.0}Ni_y$ ($y = 0$–0.4) ribbons exhibit evident steps in the demagnetized stage of the second quadrant. The H_a values of $SmCo_4B$ and $Sm_3Co_{11}B_4$ are 95.49 MA·m^{-1} and 92.31 MA·m^{-1} at 4.2 K, respectively[13]. Figure 1b shows that when $x = 1.0$ and $y = 0$–0.4, the 1:4:1, 5:19:6, and 3:11:4 phases coexist in the annealed ribbons, implying that

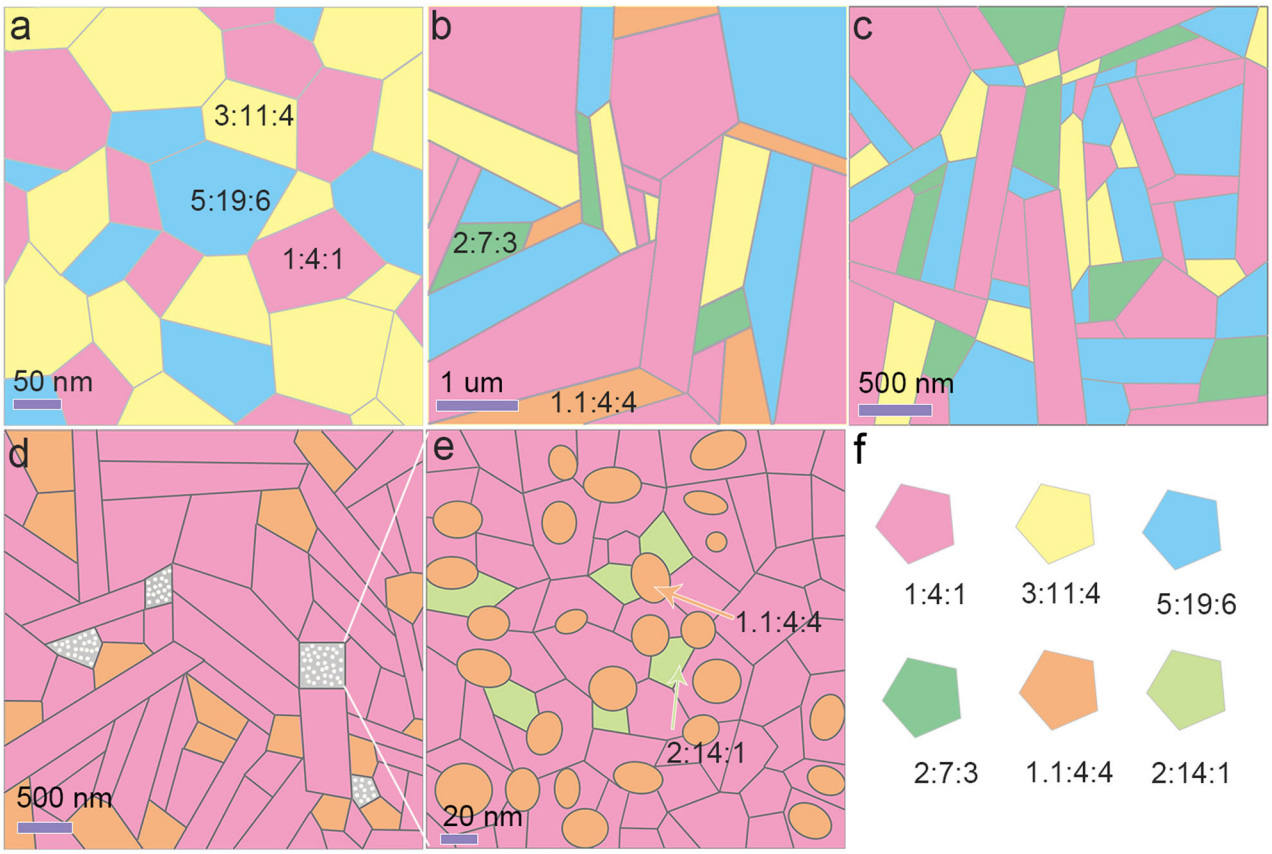

Fig. 6 | Microstructure evolution models of Fe_xNi_y ribbons after annealing at 850 °C. a $x = 1.0 - 1.2$, $y = 0 - 0.8$. **b** $x = 1.6$, $y = 0.8$. **c** $x = 1.0$, $y = 1.0$. **d** $x = 2.0$, $y = 1.0$. **e** Magnified morphology of the white region in (**d**). **f** Correspondence between color and phase.

this step should be attributed to the slight H_a difference and compositional differences in these three phases (Figs. S11–S15).

Figure 7e shows that H_c tends to increase and M_s tends to decrease with increasing Ni and Fe+Ni contents. The ribbons without Ni achieve the highest M_s of 98.0 $A \cdot m^2 \cdot kg^{-1}$, M_r of 72.7 $A \cdot m^2 \cdot kg^{-1}$, and $(BH)_{max}$ of 98.5 $kJ \cdot m^{-3}$. However, this effect is different from that of Fe + Ni on $Sm(Co_{1-x-y}Fe_xNi_y)_5$ ($x = 0.15$, $y = 0.05$; $x = 0.3$, $y = 0.1$; $x = 0.45$, $y = 0.15$)[28]. The TEM images presented in Figs. 3 and 4 show that all of the grains of the annealed Fe_xNi_y ribbons are in direct contact, and there is no second phase at the grain boundaries. The initial magnetization curves in Fig. 7a show that for all of the ribbons, the magnetization increases rapidly at low fields, exhibiting typical nucleation mechanism characteristics. Therefore, the high coercivity of the annealed Fe_xNi_y ribbons mainly originates from the high nucleation fields of the 1:4:1, 5:19:6, 2:7:3, and 3:11:4 phases. The coercivity controlled by the nucleation mechanism can be expressed by Eq. (2)[36]:

$$H_c = \alpha_k \alpha_\varphi H_a - N_{eff} M_s \quad (2)$$

Where H_a is the anisotropic field, α_k describes the effect of the inhomogeneous microstructure, α_φ quantifies the effect of the grain orientation on the coercivity, and N_{eff} is an effective demagnetization factor that depends on the grain shape. Kronmüller[37] proposed that, for a width $r_0 < \sqrt{A/K_1}$ (A and K_1 are the exchange stiffness and magnetocrystalline anisotropy constant, respectively) of the magnetic inhomogeneity region, $\alpha_k \alpha_\varphi$ is considered to be 1.0 because the grains of the annealed Fe_xNi_y ribbons are in direct contact and there are no grain boundary phases. Therefore, the H_c of annealed Fe_xNi_y ribbons mainly depends on the anisotropic field (H_a), saturation magnetization (M_s), and effective demagnetization factor (N_{eff}).

Figure 7e shows that for the $Fe_{1.0}Ni_y$ ($y = 0$–1.0) ribbons, the H_c increases with increasing Ni content until the $y = 1.0$ ribbons reach a maximum H_c of 5.68 $MA \cdot m^{-1}$, which is much higher than the highest values reported in refs. 20,21 and 3.99 $MA \cdot m^{-1}$ reporting the previous studies performed by our group[22]. Figure 1b shows that the $Fe_{1.0}Ni_y$ ($y = 0$–0.4) ribbons consist of equiaxed 1:4:1, 5:19:6, and 3:11:4 grains, and the added Ni atoms enter the Sm-Co-B phase and increase its H_a, which is similar to the substitution of Ni for Co, improving the H_a of the $Sm(Co, Ni)_5$ phase[38]. However, the magnetic moment of Ni (0.61 μ_B) is lower than that of Fe (2.2 μ_B) and Co (1.72 μ_B), so that the partial substitution of Ni for Co decreases the M_s of the Sm-Co-B phase, reducing the negative effect ($-N_{eff}M_s$) of microstructural inhomogeneity on H_c according to Eq. (2).

As y increases to 1.0, the annealed ribbons contain platelet-shaped 1:4:1, 5:19:6, 3:11:4, and 2:7:3 grains. Ni addition increases the Sm-Co-B phase H_a and promotes a change in the grain shape from equiaxed to platelet-shaped, reducing N_{eff} from nearly 1/3 in different directions to 0 in the long-axis direction of the platelet-shaped grains. Therefore, H_c is increased according to Eq. (2). In addition, Fig. 5f shows that the domain walls run through the platelet-shaped grains, and all of the grain boundaries can act as planar defects to pin the movement of the domain walls[39]. Therefore, a predominant nucleation mechanism and incidental domain-wall pinning mechanism can increase the H_c of the annealed $Fe_{1.0}Ni_{1.0}$ ribbons to 5.68 $MA \cdot m^{-1}$ at room temperature.

For the annealed $Fe_{1.2}Ni_y$ ribbons in Fig. 7c, d, H_c increases linearly from 3.46 $MA \cdot m^{-1}$ to 5.18 $MA \cdot m^{-1}$ as y increases from 0.4 to 0.8, which is attributed mainly to an enhancement of H_a of the Sm-Co-B phases.

https://doi.org/10.1038/s41467-024-54610-6

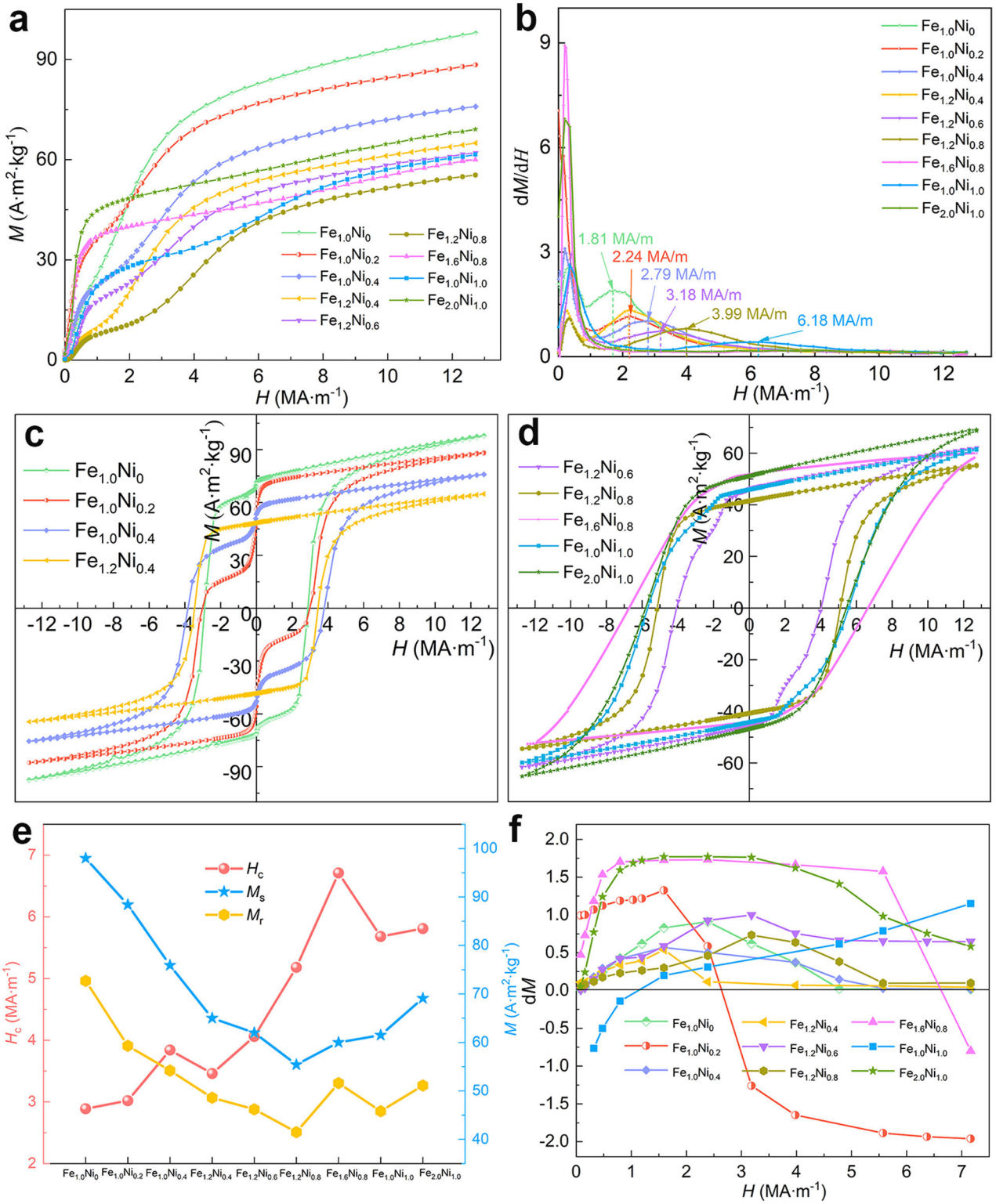

Fig. 7 | Magnetic characteristics of the ribbons annealed at 850 °C. a Initial magnetization curves of Fe_xNi_y ribbons. **b** First-order derivative curves of the initial magnetization curves. **c**, **d** Hysteresis hoops of Fe_xNi_y ribbons. **e** Magnetic property dependence of Fe_xNi_y ribbons. **f** Henkel plot curves.

For the annealed $Fe_xNi_{0.4}$ ribbons, H_c decreases from 3.84 MA·m^{-1} at $x = 1.0$ to 3.46 MA·m^{-1} at $x = 1.2$. As x increases from 1.0 to 1.2, the 3:11:4 content increases from 52.8 wt% to 78.5 wt%, the 1:4:1 content decreases from 26.4 wt% to 9.7 wt%, and the 5:19:6 content decreases from 20.8 wt% to 11.8 wt%. The cell volume of the 1:4:1 and 5:19:6 phases increases, while that of the 3:11:4 phase is essentially constant, indicating that the increased Fe mainly enters the 1:4:1 and 5:19:6 phases and saturates in the 1:4:1 phase. The dissolved Fe reduces the structural stability of the two phases. Moreover, excessive Fe reduces the K_1 of the 1:4:1 and 5:19:6 phases. Moreover, the movement of reversed domains in the mixed 1:4:1 + 5:19:6 + 3:11:4 + 2:7:3 microstructure will be pinned by phase boundaries due to the different $A \times K$

Table 2 | Magnetic parameters picked from Fig. 7c,d

Annealed ribbons	H_c (MA·m^{-1})	M_r (A · m^2·kg^{-1})	M_s (A · m^2·kg^{-1})	J_s (T)	B_r (T)	$(BH)_{max}$ (kJ·m^{-3})	M_r/M_s	Shape of grains	Coercivity mechanism
$Fe_{1.0}Ni_0$	2.89	72.7	98.0	0.94	0.68	98.5	0.74	Equiaxed	Nucleation + pinning
$Fe_{1.0}Ni_{0.2}$	3.02	59.3	88.4	0.85	0.67	83.5	0.67	Equiaxed	Nucleation + pinning
$Fe_{1.0}Ni_{0.4}$	3.84	54.2	75.9	0.73	0.56	59.5	0.71	Equiaxed	Nucleation + pinning
$Fe_{1.2}Ni_{0.4}$	3.46	48.6	65.0	0.62	0.48	43.3	0.75	Equiaxed	Nucleation + pinning
$Fe_{1.2}Ni_{0.6}$	4.06	46.2	62.0	0.59	0.45	39.1	0.75	Equiaxed	Nucleation + pinning
$Fe_{1.2}Ni_{0.8}$	5.18	41.5	55.4	0.53	0.38	31.8	0.75	Equiaxed	Nucleation + pinning
$Fe_{1.6}Ni_{0.8}$	6.71	51.6	60.0	0.57	0.50	48.4	0.86	Platelet + Equiaxed	Nucleation
$Fe_{1.0}Ni_{1.0}$	5.68	45.8	61.5	0.59	0.45	38.6	0.74	Platelet + Equiaxed	Nucleation + pinning
$Fe_{2.0}Ni_{1.0}$	5.81	51.1	69.1	0.65	0.49	46.8	0.74	Platelet + Equiaxed	Nucleation

values. According to Eq. (3)[22],

$$\Delta\gamma = 4\left(\sqrt{A_i K_i} - \sqrt{A_j K_j}\right) \tag{3}$$

Here, Δγ is the domain wall energy difference between the two phases, which is proportional to the domain wall pinning force, and the subscript $i(j)$ represents 1:4:1, 5:19:6, or 3:11:4. Because $K_{1,\ SmCo4B} > K_{1,\ Sm5Co19B6} > K_{1,\ Sm3Co11B4}$[40], excessive dissolution of Fe reduces the domain wall energy gradient between the 1:4:1, 5:19:6, and 3:11:4 phases, resulting in a decrease in H_c. The slight reduction in the magnetization of the annealed ribbons is due to the small magnetic moment of the 3:11:4 phase compared to those of the 1:4:1 and 5:19:6 phases.

For the annealed $Fe_xNi_{0.8}$ ribbons, H_c increases from 5.18 to 6.71 MA·m^{-1} as x increases from 1.2 to 1.6. Surprisingly, the annealed $Fe_{1.6}Ni_{0.8}$ ribbon shows an ultra-high H_c of up to 6.71 MA·m^{-1}. Its demagnetization curve is smooth and exhibits single hard magnetic behavior. However, the hysteresis loop is still not closed, implying that the ribbon is still not fully magnetized to saturation under the 12.73 MA·m^{-1} field. According to Fig. 1b, as x increases from 1.2 to 1.6, the 1:4:1 content increases from 11.1 wt% to 57.1 wt%, the 5:19:6 content increases from 13.5 wt% to 18.9 wt%, the 3:11:4 content decreases from 74.0 wt% to 5.4 wt%, the 1.1:4:4 phase content increases from 1.4 wt% to 13.5 wt%, and 5.1 wt% of the 2:7:3 phase (H_a = 103.45 MA·m^{-1}) is also formed. Additionally, the equiaxed grains transform into platelet-shaped grains and improve the H_c. Moreover, Fe atoms enter the Sm-Co-B phase and increase the cell volumes of the 1:4:1, 5:19:6, and 3:11:4. Therefore, when the Ni content (y) increases to 0.8, Fe addition maintains the structural stability of the 1:4:1 and 5:19:6 phases, similar to the dependence of the stability of the $SmCo_5$ phase on Ni[41]. That is, the negative impact of Fe on the structural stability of the 1:4:1 and 5:19:6 phases can be offset only when the Ni content is greater than 0.8. On the other hand, Fe addition increases the M_s and M_r values, as shown in Fig. 7e.

For the annealed $Fe_xNi_{1.0}$ ribbons, H_c increases from 5.68 MA·m^{-1} to 5.81 MA·m^{-1} as x increases from 1.0 to 2.0. Figure 1b shows that as x increases from 1.0 to 2.0, the 1:4:1 content increases from 36.6 wt% to 76.5 wt%, the 5:19:6, 3:11:4 and 2:7:3 phases disappear, and small amounts of 1.1:4:4 and 2:14:1 phases are formed. The cell volume of the 1:4:1 phase increases, which means that the increased Fe mainly enters the 1:4:1 phase. The slight increase in the H_c and magnetization of the annealed ribbons is attributed mainly to the increase in the 1:4:1 phase content.

The $\delta M - H$ or Henkel plots for all of the samples tested at 90 kOe (7.16 MA·m^{-1}) are shown in Fig. 7f. δM is defined as[42]

$$\delta M = [M_d(H) - M_r + 2M_r(H)]/M_r \tag{4}$$

Here, $M_r(H)$ and $M_d(H)$ are the remanences after applying a field (H) on a thermally demagnetized sample and after applying a reverse field on a previously saturated sample, respectively, and M_r is the saturation remanence. $\delta M > 0$ indicates strong intergranular exchange interactions, and $\delta M < 0$ indicates long-range magnetostatic interactions between grains[42].

As y increases from 0 to 0.4 with x = 1.0, y increases from 0.4 to 0.8 with x = 1.2, x increases from 1.0 to 1.2 with y = 0.4, and x increases from 1.2 to 1.6 with y = 0.8, these ribbons exhibit similar positive δM peak values (a detailed analysis is shown in Fig. S10). The $\delta M(H)$ curve of the $Fe_{2.0}Ni_{1.0}$ ribbons is similar to that of the $Fe_{1.6}Ni_{0.8}$ ribbons. δM increases linearly with increasing magnetic field and reaches a peak of 1.77 under 20 kOe (1.59 MA·m^{-1}), which is much higher than the values for the Sm-Co and Nd-Fe-B magnets reported in previous studies[42–44]. Although the $Fe_{2.0}Ni_{1.0}$ ribbons contain 19.1 wt% 1.1:4:4 paramagnetic phase, the high content of the 1:4:1 phase with high H_a prevents the formation and expansion of reversed domains and forms strong exchange coupling to achieve high coercivity. Compared with the two-stage magnetization behavior of the ribbons without platelet-shaped grains, the platelet-shaped structure contributes significantly to the strong exchange coupling between hard magnetic grains.

In this work, we achieved an ultrahigh coercivity of 2.89–6.71 MA·m^{-1} at room temperature by adjusting the amount of Fe, Co, and Ni in $SmCo_{4-x-y}Fe_xNi_yB$ ribbons. Multiphase $SmCo_{4-x-y}Fe_xNi_yB$ ribbons with platelet-shaped microstructure show a record H_c of up to 6.71 MA·m^{-1}, which is far higher than the H_c of all hard magnetic ribbons and magnets reported to date (Fig. 8). The excellent coercivity is attributed to the platelet-shaped Sm-Co-B grains with high magnetocrystalline anisotropy. However, the randomly arranged grains average the magnetization to a low value, resulting in a gap in the magnetic energy product compared to the oriented Sm-Co and Nd-Fe-B magnets. High-temperature hot deformation may be an effective approach to align hard magnetic nanograins. The anisotropic $SmCo_4B$-based magnets with a uniformly oriented platelet-shaped structure are expected to be ideal magnets for practical use.

Methods

Sample preparation

The $SmCo_{4-x-y}Fe_xNi_yB$ (x = 1.0–2.0; y = 0–1.0) alloys were prepared via vacuum smelting of high-purity Sm (99.9%), Co (99.97%), Fe (99.9%), Ni (99.95%), B powder (99.9%), and 19 wt% B-Fe alloy. An extra 10 wt% Sm was added to compensate for the Sm loss during melting. The as-cast alloys were melt-spun with a Mo wheel at a speed of 40 m · s^{-1} under high-purity argon atmosphere. Finally, the as-spun ribbons were annealed at 850 °C for 30 min to obtain the optimal magnetic properties.

Characterization

The phase composition was characterized by X-ray diffraction (XRD) using a Rigaku Dmax 2500Pc X-ray diffractometer with Cu-Ka radiation. The as-spun and annealed ribbons were ground into powder for XRD measurements in the 10–120° range, with a step of 0.02° and step

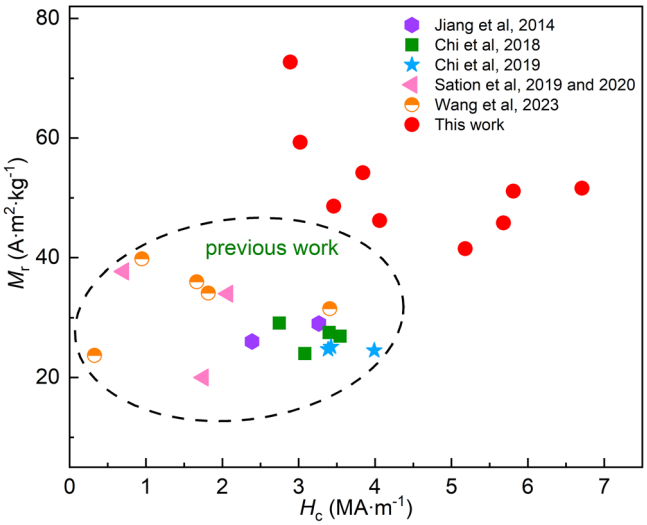

Fig. 8 | Comparison of magnetic properties between the $SmCo_4B$-based ribbons in this work and those reported in previous studies[19–22,24,45,46].

time of 3 s. The unit cell parameters and phase composition were calculated by using the FullProf Suite software. The amorphous content was calculated using the Jade software with the internal standards (search for the keyword "amorphous content" in the software help file). The amorphous content is equal to 1 minus the ratio of all diffraction peak intensities to the total intensity. The microstructure of the ribbons was observed using a JEOL JEM-F200 high-resolution transmission electron microscope (HRTEM), and the domain structure was characterized using a JEOL 2100 F Lorentz TEM instrument (LTEM). The ribbon samples for TEM observation were prepared using a focused ion beam scanning electron microscope (FIB-SEM, Hitachi Ethos NX5000). The magnetic properties of the annealed ribbons were measured using a physical property measurement system (PPMS, Cryogenic CFMS-16 T) with a maximum field of 16 T (~ 12.73 MA·m^{-1}), and the applied magnetic field was perpendicular to the surface of the ribbons.

Data availability

The raw XRD, DSC, and PPMS data generated in this study have been deposited in the Mendeley Data [Sun, Ji-bing(2024),"High-performance multiphase Sm-Co-B alloys with a coercivity up to 6.71 MA/m", MendeleyData, VI, doi: 10.17632/xm5k8hny29.1]. The other image data are provided in the main text and Supplementary Information. All other information can be obtained from the corresponding author upon request.

References

1. Coey, J. M. D. Perspective and prospects for rare earth permanent magnets. *Engineering* **6**, 119–131 (2020).
2. Gutfleisch, O. et al. Magnetic materials and devices for the 21st century: stronger, lighter, and more energy efficient. *Adv. Mater.* **23**, 821–842 (2011).
3. Xu, K. et al. Design of the rare-earth-containing materials based on the micro-alloying phase equilibria, phase diagrams and phase transformations. *J. Mater. Sci. Technol.* **151**, 119–149 (2023).
4. Chen, H. et al. Strategy and mechanism for substantially enhanced coercivity in multi-main-phase Nd-La-Ce-Fe-B sintered magnets. *Acta Mater.* **261**, 119408 (2023).
5. Liu, J., Walmer, M. & Jasinski, M. In *Modern Permanent Magnets* 113–134 (Woodhead Publishing, 2022).
6. Coey, J. M. D. Permanent magnet applications. *J. Magn. Magn. Mater.* **248**, 441–456 (2002).
7. Magnetics, D. Available samarium cobalt magnet grades: samarium cobalt. https://www.duramag.com/samarium-cobalt-magnets-smco/available-samarium-cobalt-magnet-grades.
8. Wang, D. et al. Exchange-coupled nanoscale SmCo/NdFeB hybrid magnets. *J. Magn. Magn. Mater.* **324**, 2836–2839 (2012).
9. Teng, Y. et al. Microstructure evolution of hot-deformed SmCo-based nanocomposites induced by thermo-mechanical processing. *J. Mater. Sci. Technol.* **138**, 193–202 (2023).
10. Matsuura, Y. Recent development of Nd-Fe-B sintered magnets and their applications. *J. Magn. Magn. Mater.* **303**, 344–347 (2006).
11. Kaneko, Y. Highest performance of Nd-Fe-B magnet over 55 MGOe. *IEEE Trans. Magn.* **36**, 3275–3278 (2000).
12. Strnat, K., Hoffer, G., Olson, J., Ostertag, W. & Becker, J. A family of new cobalt base permanent magnet materials. *J. Appl. Phys.* **38**, 1001–1002 (1967).
13. Ido, H. et al. Magnetic study of $Sm_{n+1}Co_{3n+5}B_{2n}$ (n = 0,1,2,3) in a pulsed high field. *Physica B* **177**, 265–269 (1992).
14. Chen, Y. et al. Phase relation in the system Sm-Co-B. *J. Alloys Compd.* **305**, 216–218 (2000).
15. Liu, J. P., de Boer, F. R. & Buschow, K. H. J. Exchange interaction in rare-earth compounds of the type RCo_4B. *J. Less Common Met.* **175**, 137–141 (1991).
16. Burzo, E. In *Rare earths-transition metals-boron compounds: basic properties to technical applications*. 211–376 (Springer International Publishing, 2023).
17. Chi, X. et al. A comparative study on structures and magnetic properties of $SmCo_4B$ and $SmCo_{3.1}Fe_{0.9}B$ ribbons. *Physica B* **545**, 176–181 (2018).
18. Ido, H., Ogata, H. & Maki, K. Magnetic characteristics of the $Sm_{1-x}Pr_xCo_{4-y}Fe_yB$ system. *J. Appl. Phys.* **73**, 6269–6271 (1993).
19. Jiang, X., Devaraj, A., Balamurugan, B., Cui, J. & Shield, J. E. Microstructure of multistage annealed nanocrystalline $SmCo_2Fe_2B$ alloy with enhanced magnetic properties. *J. Appl. Phys.* **115**, 063902 (2014).
20. Jiang, X., Balamurugan, B. & Shield, J. E. Effect of Fe content on structural and magnetic properties of $SmCo_{4-x}Fe_xB$ alloys. *J. Alloys Compd.* **617**, 479–484 (2014).
21. Saito, T. & Nishio-Hamane, D. Synthesis of $Sm(Co,Fe)_4B$ compounds by rapid quenching and subsequent heat treatment. *Intermetallics* **107**, 6–9 (2019).
22. Chi, X., Sun, J. B., Wang, S., Wang, H. W. & Zhang, Y. Effect of Fe content on the structure and magnetic properties of $SmCo_{3.94-x}Fe_xCu_{0.06}B$ ribbons. *J. Appl. Phys.* **125**, 235106 (2019).
23. Chi, X. et al. A new $Sm(Co,Fe,Cu)_4B/Sm_2(Co,Fe,Cu)_7$ cell structure with the coercivity of up to 5.01 T. *J. Magn. Magn. Mater.* **458**, 66–74 (2018).
24. Chi, X. et al. Effect of Cu addition on the structure and magnetic properties of $SmCo_{3.1-x}Fe_{0.9}Cu_xB$ ribbons. *J. Magn. Magn. Mater.* **465**, 524–530 (2018).
25. Landa, A. et al. Thermodynamics of $SmCo_5$ compound doped with Fe and Ni: An ab initio study. *J. Alloys Compd.* **765**, 659–663 (2018).
26. Söderlind, P. et al. Prediction of the new efficient permanent magnet $SmCoNiFe_3$. *Phys. Rev. B* **96**, 100404 (2017).
27. Coey, J. M. D. Hard magnetic materials: a perspective. *IEEE Trans. Magn.* **47**, 4671–4681 (2011).
28. Gavrikov, I. S. et al. Effect of Ni doping on stabilization of $Sm(Co_{1-x}Fe_x)5$ compound: thermodynamic calculation and experiment. *J. Phys.: Condens. Matter* **32**, 425803 (2020).
29. Access to the website: https://next-gen.materialsproject.org/about/cite.
30. Bezinge, A., Braun, H. F., Muller, J. & Yvon, K. Tetragonal rare earth (R) Iron borides, $R_{1+\varepsilon}Fe_4B_4$ ($\varepsilon \simeq 0.1$), with incommensurate rare earth and iron substructures. *Solid State Commun.* **55**, 131–135 (1985).

31. Zhao, M. et al. Origin and inhibition on quasi-periodic coarse grain regions in hot-deformed Nd-Fe-B magnets. *Acta Mater.* **255**, 119070 (2023).
32. Xia, X. et al. Significant enhancement in the coercivity and thermal stability of bulk hot-deformed Nd-Fe-B magnets by intergranular addition of Nd-Dy/Tb-Cu-Ga alloys. *Acta Mater.* **232**, 117945 (2022).
33. Chen, Y. et al. Syntheses and magnetic properties of $R_{m+n}Co_{5m+3n}B_{2n}$ compounds. *J. Phys. Condens. Matter* **11**, 8251–8261 (1999).
34. Guimares, A. P. *Principles of Nanomagnetism* (NanoScience and Technology, 2009).
35. Ido, H., Nashima, O., Takahashi, T., Oda, K. & Sugiyama, K. New magnetic material based on $SmCo_4B$. *J. Appl. Phys.* **76**, 6165–6167 (1994).
36. Kronmüller, H., Durst, K. D. & Sagawa, M. Analysis of the magnetic hardening mechanism in RE-FeB permanent magnets. *J. Magn. Magn. Mater.* **74**, 291–302 (1988).
37. Kronmüller, H. Theory of nucleation fields in inhomogeneous ferromagnets. *Phys. Stat. Sol. B* **144**, 385–396 (1987).
38. Ermolenko, A. S. Magnetocrystalline anisotropy of rare earth intermetallics. *IEEE Trans. Magn.* **12**, 992–996 (1976).
39. Balamurugan, B., Sellmyer, D. J., Hadjipanayis, G. C. & Skomski, R. Prospects for nanoparticle-based permanent magnets. *Scripta Mater.* **67**, 542–547 (2012).
40. Chi, X. et al. Microstructure and magnetic properties of $Sm_3Co_{11-x}Fe_xB_4$ ribbons with superior coercivity. *J. Alloys Compd.* **942**, 169107 (2023).
41. Antoniou, E. et al. Structural and magnetic properties of $SmCo_{5-x}Ni_x$ intermetallic compounds. *J. Alloys Compd.* **882**, 160699 (2021).
42. Bolyachkin, A. S., Alekseev, I. V., Andreev, S. V. & Volegov, A. S. δM plots of nanocrystalline hard magnetic alloys. *J. Magn. Magn. Mater.* **529**, 167886 (2021).
43. Huang, G. et al. Engineering bulk, layered, multicomponent nanostructures with high energy density. *Small* **14**, 1800619 (2018).
44. Wang, K. et al. Effect of Cu addition on the microstructure and magnetic properties of the Nd-Fe-B melt-spun ribbons. *J. Supercond. Nov. Magn.* **34**, 3369–3376 (2021).
45. Saito, T. & Nishio-Hamane, D. Synthesis of high-coercivity (Y,Sm)Co_2Fe_2B nanomaterials. *J. Magn. Magn. Mater.* **494**, 165767 (2020).
46. Wang, S., Sun, J. B., Chi, X., Zhou, M. J. & Li, X. M. Microstructure evolution of Pr-doped $SmCo_4B$-based ribbons with improved magnetization. *J. Alloys Compd.* **956**, 170266 (2023).

Acknowledgements

This work was supported by the National Natural Science Foundation of China (NNSFC) (No. 52371185 to J.B.S., 52271195 to Y.Z.), Guangdong Basic and Applied Basic Research Foundation, China (2021A1515110113 to X.C.), the Natural Science Foundation of Hebei Province, China (No. E2022202017 to J.B.S.), the S&T Program of Hebei (22567635H to J.B.S.), and the CAS Project for Young Scientists in Basic Research (YSBR-084 to Y.Z.).

Author contributions

S.W. conducted experiments, wrote and prepared the manuscript. J.B.S. provided conceptualization, methodology, supervision, reviewing and editing. X.C. conducted TEM experiments and performed data analysis. M.J.Z. conducted micromagnetic simulation. H.Y.M. conducted experiments. Y.Z. performed the external validation, Lorentz transmission electron microscopy observation and analysis, and contributed to the discussion of the results. Jian Liu provided methodological support and contributed to the discussion of the results. All authors read, revised, and approved the manuscript.

Competing interests

The authors declare no competing interests.

Ethical approval

We have complied with all relevant ethical regulations.

Additional information

Supplementary information The online version contains supplementary material available at https://doi.org/10.1038/s41467-024-54610-6.

Correspondence and requests for materials should be addressed to Ji-Bing Sun, Xiang Chi, Ying Zhang or Jian Liu.

Peer review information *Nature Communications* thanks Margarit Gjoka, and the other, anonymous, reviewer(s) for their contribution to the peer review of this work. A peer review file is available.